arXiv:2301.12840v2 [cond-mat.mtrl-sci] 22 Jun 2023

On energetics of allotrope transformations in transition-metal diborides via plane-by-plane shearing

Thomas Leiner,[1,*] Nikola Koutná,[2,3] Jozef Janovec,[4,5] Martin Zelený,[5] Paul H. Mayrhofer,[2] and David Holec[1]

[1] *Department of Materials Science, Montanuniversität Leoben, Leoben, Austria*
[2] *Institute of Materials Science and Technology, TU Wien, Vienna, Austria*
[3] *Department of Physics, Chemistry, and Biology (IFM), Linköping University, Linköping, Sweden*
[4] *Centro de Física de Materiales-MPC CSIC-UPV/EHU, San Sebastián, Spain*
[5] *Institute of Materials Science and Engineering, Faculty of Mechanical Engineering, Brno University of Technology, Brno, Czech Republic*

(Dated: June 23, 2023)

Transition metal diborides crystallize in the α, γ, or ω type structure, in which pure transition metal layers alternate with pure boron layers stacked along the hexagonal [0001] axis. Here we view the prototypes as different stackings of the transition metal planes and suppose they can transform from one into another by a displacive transformation. Employing first-principles calculations, we simulate sliding of individual planes in the group IV–VII transition metal diborides along a transformation pathway connecting the α, γ, and ω structure. Chemistry-related trends are predicted in terms of energetic and structural changes along a transformation pathway, together with the mechanical and dynamical stability of the different stackings. Our results suggest that MnB_2 and MoB_2 possess the overall lowest sliding barriers among the investigated TMB_2s. Furthermore, we discuss trends in strength and ductility indicators, including Young's modulus or Cauchy pressure, derived from elastic constants.

I. INTRODUCTION

Transition metal diborides (TMB_2s) are a vibrant research topic in application-oriented coating developments [1–6] and represent promising materials for usage in extreme environments, including ultra-high temperatures and severe mechanical loads. Among their attractive properties are chemical stability and inertness, high melting point, high hardness, good electrical and thermal conductivity, corrosion, and erosion resistance as well as high wear and thermal-shock resistance [7, 8]. TMB_2s with extraordinary characteristics include TaB_2 and ReB_2—showing hardness values up to 46–49 GPa [9] and 48 GPa [10], respectively—or e.g. MgB_2, which is a superconductor with a critical temperature of 39 K [11]. Among the most widely researched diborides is TiB_2[12, 13], valued for its high chemical stability and high melting point (3500 K), high hardness (24 GPa) and chemical inertness, as well as electric resistivity and thermal conductivity [14]. High hardness (26 GPa) and low electrical resistivity is reported also for WB_2, applicable as a conductor under extreme conditions [15].

TMB_2s are known to commonly crystallize in layered structures with hexagonal symmetry, most often in the AlB_2-type phase (α, space group #191–P6/mmm) which is typical for diborides of early transition metals [7]. Furthermore, the ReB_2-type phase (γ, space group #194–$P6_3/mmc$) has been reported for ReB_2 [16] and the WB_2-type phase (ω, space group #194–$P6_3/mmc$) can be stabilized for late TMB_2s [17]. All three phases—α, γ, and ω—can be viewed as layered structures that alternate hexagonal nets of pure TM atoms and layers of pure B atoms (arranged in honeycombs), stacked along the c-axis. Using the standard labeling for stacking of hexagonal planes, the arrangement of the metal atoms can be described as A-A-A-A, A-B-A-B, and A-A-B-B stacking sequence for the α, γ, and ω phase, respectively. The boron sheets between the metal planes come in two configurations: either flat (H) as in the α phase, or puckered (K) as in the γ phase. Using this nomenclature, first introduced by Kiessling *et al.* [18], the 3 structural prototypes are described as:

α: ...-A-H-$\overbrace{\text{A-H-A-H-A-H-A-H}}$-A-H-... ,
γ: ...-B-K-$\overbrace{\text{A-K-B-K-A-K-B-K}}$-A-K... ,
ω: ...-B-K-$\overbrace{\text{A-H-A-K-B-H-B-K}}$-A-H... .

The structures, therefore, do not only differ by the stacking of the metal planes (A, B) but also by the geometry of the boron planes. While these are all flat in the α structure, they are all puckered in the γ structure. The ω phase contains alternating flat and puckered boron sheets. It is interesting to observe that the flat H configuration of B planes always appears when the surrounding metal planes have the same stacking (i.e. A-A or B-B). We note that the above formalism allows also for other stackings, e.g., ...-A-H-A-K-B-H-B-K-C-H-C-K-... (structure of Mo_2B_5 [16]) which are, however, not the focus of the present work.

The fact that the three prototypes differ primarily by the stacking of the TM planes provokes the idea that they can transform from one into another by shearing/sliding individual planes, i.e. by a displacive transformation. This corresponds to the $(0001)[1\bar{1}00]$ slip, previously identified as the origin of easy plasticity of ReB_2 [19] and later found active also in ZrB_2 [20]. We note that

* thomas.leiner@unileoben.ac.at

other slip systems, such as $(1\bar{1}00)[11\bar{2}3]$ or $(0001)[11\bar{2}0]$, may be operative for different TMB_2s depending on temperature [21].

In this work, we simulate sliding of individual planes in TMB_2s using first-principles calculations. We aim to provide chemistry-related trends for 12 group IV–VII transition metal diborides in terms of their stability, as well as energetic and structural changes along a transformation pathway connecting all three prototypes, namely, AAAA → BAAA → ABAB → ABBA → AAAA. Here AAAA, ABAB, and ABBA correspond to the metal plane stackings in the α, γ, and ω structures, respectively.

II. METHODS

The calculations were performed using the Vienna *ab-initio* Simulation Package (VASP) [22] using the projector-augmented wave (PAW) method and a plane wave basis set [23]. The exchange-correlation effects were treated with the aid of generalized gradient approximation (GGA) functionals from Perdew-Burke-Ernzerhof (PBE) [24]. The Γ-centered k-point mesh was automatically generated with a length parameter of 50 Å while the plane waves cut-off energy was set to 500 eV.

The simulation cells consist of four metal layers and four boron layers and, therefore, 12 atoms each. Geometric constraints were set using the GADGET code by Bučko *et al.* [25]. Specifically, all structures were allowed to relax in the a- and c-direction, while keeping the lattice angles α, β and γ at 90° and 120°, respectively, to preserve the hexagonal crystal symmetry. Boron atoms were allowed to move freely, whereas metal atoms could move only along the [0001] (c) direction. All systems (including CrB_2 and MnB_2) were treated as non-magnetic. The energy barrier between stackings $\mathcal{S}_1$ (e.g. AAAA) and $\mathcal{S}_2$ (e.g. BAAA) a is calculated as

$$E(\mathcal{S}_1 \to \mathcal{S}_2) = \begin{cases} E_{\text{tot}}^{\max} - E_{\text{tot}}^{\min}, & \text{if } E_{\text{tot}}(\mathcal{S}_1) < E_{\text{tot}}(\mathcal{S}_2) \\ E_{\text{tot}}^{\max} - E_{\text{tot}}(\mathcal{S}_1), & \text{otherwise,} \end{cases} \tag{1}$$

where $E_{\text{tot}}^{\max}$ ($E_{\text{tot}}^{\min}$) is the maximal (minimal) total energy along the $\mathcal{S}_1 \to \mathcal{S}_2$ pathway, and $E_{\text{tot}}(\mathcal{S}_1)$, $E_{\text{tot}}(\mathcal{S}_2)$ are total energies of $\mathcal{S}_1$ and $\mathcal{S}_2$, respectively. We note that Eq. (1) allows to resolve directionally-dependent barriers, i.e. $E(\mathcal{S}_1 \to \mathcal{S}_2)$ is generally different from $E(\mathcal{S}_2 \to \mathcal{S}_1)$.

To assess mechanical stability and predict trends in elastic properties, the stress-strain method [26–28] was used to calculate fourth-order elasticity tensors, mapped onto symmetric 6×6 matrices of elastic constants, $\{C_{ij}\}$, via Voigt's notation. Subsequently, positive definiteness of the $\{C_{ij}\}$ matrix (equivalent to the positivity of its minimal eigenvalue) served as a necessary and sufficient criterion for the mechanical stability of the corresponding structure [29]. Imposing the macroscopic symmetry, elastic matrices were projected on those of a hexagonal system thus yielding five independent elastic constants (C_{11}, C_{12}, C_{13}, C_{33}, and C_{44}). The polycrystalline Young's modulus, $E = 9BG/(3B+G)$ was calculated using the Hill's average of the bulk, B, and shear modulus, G [30, 31].

Furthermore, dynamical stability was addressed through calculating phonon spectra, using the Phonopy package [32] with a 4×4×1 (192-atom) replica of the fully relaxed diboride simulation cell, using the small displacements method with the default displacement of 0.01 Å. To analyze the chemical bonding, we take advantage of the crystal orbital Hamilton population (COHP) [33]—a tool that weights the density of states (DOS) by the elements of the Hamilton matrix—calculated within the LOBSTER package [34] capable of extracting chemical information from plane-wave wave function by its transformation onto a local basis set [35].

III. RESULTS AND DISCUSSION

A. Transformation energy landscape

First we discuss total energy (E_{tot}) variations along the AAAA–BAAA–BABA–ABBA–AAAA transformation pathway (Fig. 1a), visualized in a relative comparison with the energy of the AAAA stacking,

$$\Delta E_{\text{tot}} = E_{\text{tot}} - E_{\text{tot}}(\text{AAAA}) \ . \tag{2}$$

Groups IV and V TMB_2s yield positive ΔE_{tot} along the entire deformation path indicating that the AAAA stacking is the most stable one. In contrast, virtually zero (see e.g. BAAA-CrB_2) or even largely negative ΔE_{tot} values (see e.g. BABA-ReB_2) calculated for the group VI and VII TMB_2s suggest comparable energetic preference or even a strong tendency for other stackings than the AAAA one. This indication is further underpinned by the stability analysis (Fig. 1b) revealing that the AAAA allotrope is dynamically or even mechanically unstable (AAAA-ReB_2) for the group VI and VII TMB_2s.

Trends in the total energy variations (Fig. 1a) almost perfectly follow the left-to-right (group IV→VII) and top-to-bottom (period 4→6) move in the periodic table. Specifically, ΔE_{tot} along the entire deformation pathway generally decreases when moving from the group IV (e.g. Ti) to VII (e.g. Re) transition metals—thus, when increasing the number of valence electrons—but also within each group when changing from the period 4 (e.g. V) to 6 (e.g. Ta)—thus, when increasing the number of electron shells. Starting with the group IV TMB_2s—TiB_2, ZrB_2, and HfB_2—Fig. 1a indicates a strong preference for the AAAA stacking, since both BAAA and ABBA yield E_{tot} of about 0.28 eV/at. higher, and BABA shows E_{tot} even ≈ 0.5 eV/at. above that of AAAA. The almost overlapping energy landscapes of TiB_2, ZrB_2, and HfB_2 suggest basically no effect of changing the period (Ti→Zr→Hf). The group V TMB_2s—VB_2, NbB_2, and TaB_2—nearly mirror the ΔE_{tot} profile predicted for the group IV TMB_2s, however, all energies are shifted to

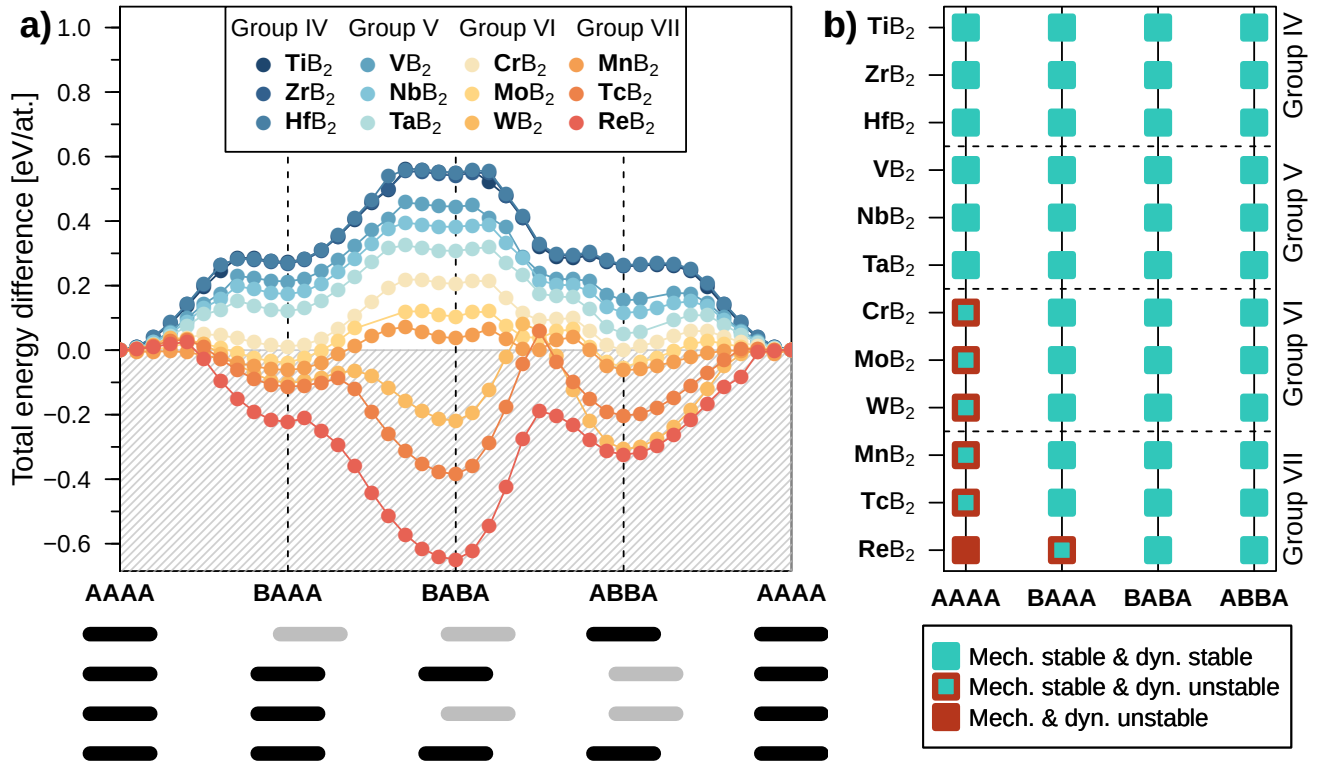


FIG. 1. (a) Total energy difference, $\Delta E_{\rm tot}$, of TMB_2 structures (where TM are group IV–VII transition metals), with various stackings compared to the reference AAAA stacking. The data points in-between stackings AAAA, BAAA, BABA, and ABBA correspond to step-wise shifts of the respective metallic plane(s) as schematically shown below the x-axis. (b) Mechanical and dynamical stability of TMB_2 structures with AAAA, BAAA, BABA, and ABBA stacking sequences, respectively.

lower values. Additionally, we observe a systematic $E_{\rm tot}$ decrease for V→Nb→Ta, i.e. upon changing the period 4→5→6. While the BABA stacking is still the least stable one ($\Delta E_{\rm tot} \approx 0.3$–$0.45$ eV/at.), the energy profile becomes asymmetric due to a slight preference of the ABBA ($\Delta E_{\rm tot} \approx 0.07$–$0.16$ eV/at.) over BAAA ($\Delta E_{\rm tot} \approx 0.16$–$0.21$ eV/at.) stacking. This is likely related to the fact that the former, ABBA, stacking is more symmetric than the BAAA one. Despite relatively high energies of the BAAA, BABA, and ABBA stackings for the group IV and V transition metal diborides, they are all found dynamically stable (Fig. 1b).

Moving to the group VI TMB_2s—CrB_2 (treated as non-magnetic), MoB_2, and WB_2—$\Delta E_{\rm tot}$ shifts to even lower values, hence, changing the order of stability of the four allotropes (note that the AAAA stacking becomes dynamically unstable, cf. Fig. 1b). With essentially zero $\Delta E_{\rm tot}$ predicted for BAAA-CrB_2 and ABBA-CrB_2, the BAAA and ABBA stackings are energetically equivalent to AAAA, but are dynamically stable in contrast to the AAAA stacking. Due to their negative $\Delta E_{\rm tot}$ values (approx. -0.04 and -0.05 eV/at., respectively), the BAAA and ABBA variants of MoB_2 are even energetically preferred over the AAAA, and the ABBA stacking becomes the new lowest-energy allotrope. With $\Delta E_{\rm tot} \approx -0.31$ eV/at., the ABBA stacking is the most stable variant also for WB_2. This is consistent with previous DFT calculations reporting that WB_2 prefers to crystallize in the ω-type phase [36]. As $\Delta E_{\rm tot}$(BAAA-WB_2)≈ -0.10 eV/at. and $\Delta E_{\rm tot}$(BABA-WB_2)≈ -0.22 eV/at., the BABA allotrope, which was the least stable one for the groups IV and V TMB_2, is more stable than both the AAAA and BAAA variants.

Since CrB_2 [37] and MnB_2 [38] have been reported as being ferromagnetic (in the AAAA structure), we have also calculated their total energies in the AAAA, BABA, and BBAA configurations. For all stackings, the total energy decreased with respect to the non-magnetic configurations. More importantly, for CrB_2 the most stable allotrope changed from the AAAA to the ABBA stacking, whereas for MnB_2, it changed from the ABBA to the BABA structure. However, the magnetic degree of freedom adds huge complexity to the simulation protocol along the whole transformation path, which goes beyond the scope of the present overview study and hence will not be discussed anymore.

Fig. 1b summarizes the mechanical and dynamical stability of the investigated stacking. The only mechanically unstable system is ReB_2 in the AAAA stacking, failing the condition $C_{44} > 0$ [29]. This suggests that the AAAA-ReB_2 is unstable with respect to shear in the $y-z$ and $x-z$ planes. And indeed, its stable configura-

tion is the ABAB stacking (Fig. 1a): the local stacking change AA→AB indeed corresponds to the out-of-plane shear $y-z$ or $x-z$ (or their combination).

The group VII TMB_2s—MnB_2 (treated as non-magnetic), TcB_2 (included for completeness but never experimentally reported), and ReB_2—yield mostly negative $\Delta E_{\rm tot}$ values along the entire transformation pathway. Similarly to the group VI TMB_2s, the AAAA allotrope is dynamically unstable. MnB_2 yields the lowest $\Delta E_{\rm tot}$ (≈ -0.06 eV/at.) for the ABBA stacking, closely followed by BAAA. TcB_2 and ReB_2 exhibit very deep global energy minima at the BABA stacking, with $\Delta E_{\rm tot}$ of -0.38 and -0.65 eV/at., respectively. This agrees well with the previously reported preference of ReB_2 for the γ-type phase [39]. Also the BAAA and ABBA allotropes of ReB_2 show low $\Delta E_{\rm tot}$ values, both below -0.2 eV/at., however, the former is predicted to be dynamically unstable.

Fig. 2a–h depict energy barriers, E-barriers (for definition, please see Eq. (1) in the Methods), that need to be overcome when changing between the AAAA, BAAA, BABA, and ABBA diboride allotropes.

The AAAA→BAAA transformation (Fig. 2a) comes with high energetic costs (0.28–0.29 eV/at.) for the group IV TMB_2, decreasing for the group V TMB_2 (0.23–0.15 eV/at. for V→Nb→TaB_2), and almost diminishing for the group VI and VII TMB_2, which fall down to 0–0.05 eV/at. Conversely, the BAAA→AAAA transition (Fig. 2b) is energetically cheap for the group IV and V TMB_2 (0.01–0.03 eV/at.) and becomes more costly for their group VI–VII counterparts, with the highest barrier of ≈ 0.25 eV/at. predicted for ReB_2.

The barrier associated with the BAAA→BABA transition (Fig. 2c) is again the highest for the group IV TMB_2 (0.29 eV/at.) and decreases down to 0.01 eV/at. when moving to the right in the periodic table, i.e. to the group VII TMB_2. It also decreases within each group (with MnB_2 being the only outlier from this trend). Transformation in the opposite direction, BABA→BAAA (Fig. 2d), presents basically no energetic barrier (0.01–0.02 eV/at.) for the group IV–VI TMB_2—excluding WB_2 with E-barrier of 0.16 eV/at.—while the same transition becomes very costly for TcB_2 and ReB_2 (with E-barrier above 0.3 eV/at.).

For the group IV–V TMB_2 together with CrB_2 and MoB_2, the BABA→ABBA transition (Fig. 2e) requires the energy of only 0.01–0.02 eV/at., while the reverse ABBA→BABA is associated with a barrier of 0.17–0.3 eV/at. Both the BABA→ABBA and ABBA→BABA transitions are relatively costly (above 0.13 eV/at.) for TcB_2 and ReB_2.

Finally, the ABBA→AAAA and AAAA→ABBA (Fig. 2g–h) energy barriers for the group IV TMB_2 are 0.01 and 0.27 eV/at., respectively, underpinning the strong preference for AAAA stacking. The ABBA→AAAA transition is cheap also for the group V TMB_2 (E-barrier of 0.02–0.06 eV/at.), while the AAAA→ABBA again comes at higher energetic costs (0.18–0.11 eV/at.). CrB_2 presents the borderline with nearly the same barriers (0.06 eV/at.) for the ABBA→AAAA and AAAA→ABBA transformation. Afterward going to MoB_2, WB_2, MnB_2, TcB_2, and ReB_2, the AAAA→ABBA transition is associated with much lower barrier compared to the ABBA→AAAA transition.

We note that since the AAAA stacking is dynamically unstable for the group VI–VII TMB_2, barriers involving the AAAA structure of those systems should be taken with a grain of salt; instead, we propose that a direct transition BAAA↔BBAA (which is due to periodic boundary conditions equivalent with the ABBA stacking) will take place, presumably yielding lower barriers than the ABBA↔AAAA↔BAAA ones.

To interpret the transformation energetics in terms of mechanical loading, we considered the supercell as a solid box composed of four blocks. During each transformation step, one or two of these blocks "move" (cf. the scheme in Fig. 1a). The motion of a block i can be viewed as a consequence of an applied horizontal force F_i acting along the $\langle 1\bar{1}00\rangle$ direction. When a block i changes its stacking type during the transformation step, i.e. $A \to B$ or $B \to A$, the force F_i facilitates work W_i along the path of a length $|\langle 1\bar{1}00\rangle|a/3 = \sqrt{3}a/3$, that is

$$W_i(x) = \int_0^x F_i(\xi)\frac{\sqrt{3}a}{3}d\xi \ . \tag{3}$$

If the stacking does not change, the path has a zero length and no work is done. The total energy change along the transformation path (Eq. 1) equates to a sum of the W_i contributions, i.e. the work done starting from the initial AAAA configuration,

$$\Delta E_{\rm tot}(x) = \sum_{i=1}^{4} W_i(x) \ . \tag{4}$$

Considering the mirror symmetry of the simulation box, the instantaneous magnitudes of the acting forces (i.e. acting on moving blocks) are the same. Therefore, the force magnitude can be obtained as a derivative of the energy

$$F(x) = \frac{1}{n}\cdot\frac{3}{\sqrt{3}a}\cdot\frac{d}{dx}\left(\Delta E_{\rm tot}(x)\right) \ , \tag{5}$$

where the multiplicity factor n (the number of moving blocks) is 1 along the AAAA↔BAAA↔BABA pathways, and 2 otherwise. Finally, we recalculate the force $F(x)$ (Eq. 5), to the applied normal stress, σ in the $\langle 1\bar{1}00\rangle$ direction by dividing $F(x)$ by the normal area A of the block,

$$\sigma(x) = \frac{F(x)}{A} = F(x)\cdot\frac{4}{ac} \ , \tag{6}$$

where c is the simulation box length along the [0001] direction for the reference AAAA stacking. The resulting $\sigma(x)$ profile is shown in Fig. 2i, indicating that the maximum stresses along the AAAA→BAAA→BABA path

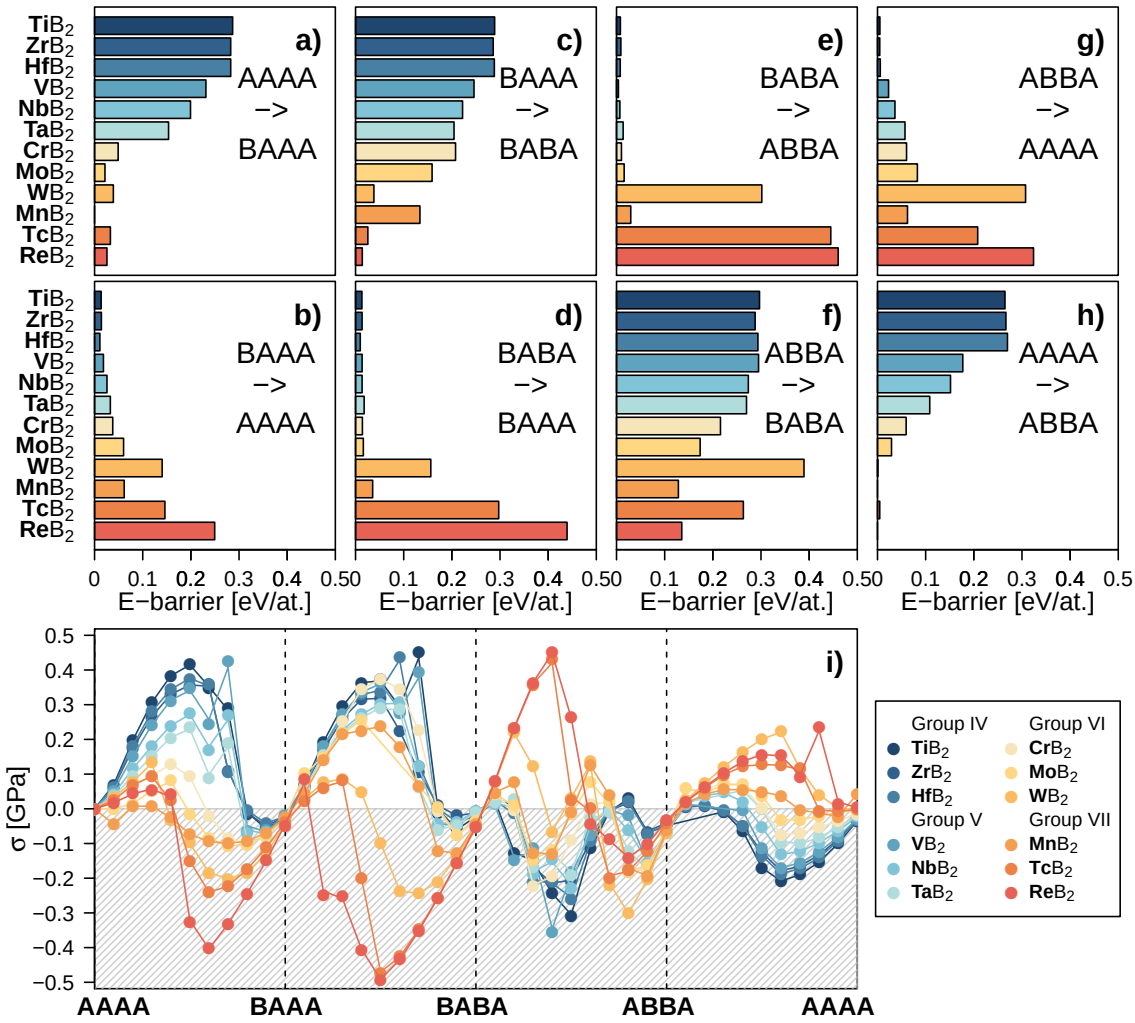


FIG. 2. Energy barriers (defined by Eq. 1) for the (a) AAAA→BAAA, (b) BAAA→BAAA, (c) BAAA→BABA, (d) BABA→BAAA, (e) BABA→ABBA, (f) ABBA→BABA, (g) ABBA→AAAA, (h) AAAA→ABBA transitions. (i) The normal stress, σ_{xx} (defined by Eq. 6), along the $\langle 1\bar{1}00 \rangle$ direction plotted in relative comparison to the AAAA stacking.

are larger than for AAAA→ABBA→BABA transformation path for all group IV and V TMB_2, as well as for CrB_2, MoB_2 and MnB_2. This suggests that the $\alpha \to \gamma$ transformation—when facilitated by normal stresses and related shuffling of planes—may proceed differently for different TMB_2. Unlike that, the $\alpha \to \omega$ transformation is predicted to always proceed directly AAAA→ABBA, rather than via the γ BABA stacking. The lowest transformation stress is predicted for ReB_2: 0.09 GPa for the $\alpha \to \gamma$ and 0.03 GPa for $\alpha \to \omega$ transformations. However, the most stable configuration of the ReB_2 is the BABA stacking; the transformation stresses from $\gamma \to \alpha$ and $\gamma \to \omega$ reach over 0.4 GPa, thus making this allotrope extremely stable, once formed. On the contrary, TiB_2 yields the largest transformation stress for the $\alpha \to \omega$ (0.21 GPa), whereas for the $\alpha \to \gamma$ transformation, the maximum stress is obtained for VB_2 (0.36 GPa) proceeding via the ABBA (ω) stacking.

B. Structural changes

Energy variations along the AAAA–BAAA–BABA–ABBA–AAAA transformation pathway can be further understood in view of the underlying structural changes (Fig. 3). In particular, different stacking sequences on the metal sublattice are followed by (partial) puckering of the boron hexagons and, consequently, volumetric changes.

Fig. 3a depicts relative volume (V) increase/decrease in comparison with the AAAA stacking. The group IV–V transition metal diborides yield the overall lowest volume for the AAAA stacking, earlier identified as their lowest-energy allotrope (Fig. 1a). Furthermore, these diborides exhibit a volume increase along the entire deformation pathway, with maximum volume (i.e. the lowest density) predicted for the energetically least favorable BABA stacking. For illustration, the AAAA→BAAA and AAAA→ABBA TiB_2 transitions lead to ≈ 5% vol-

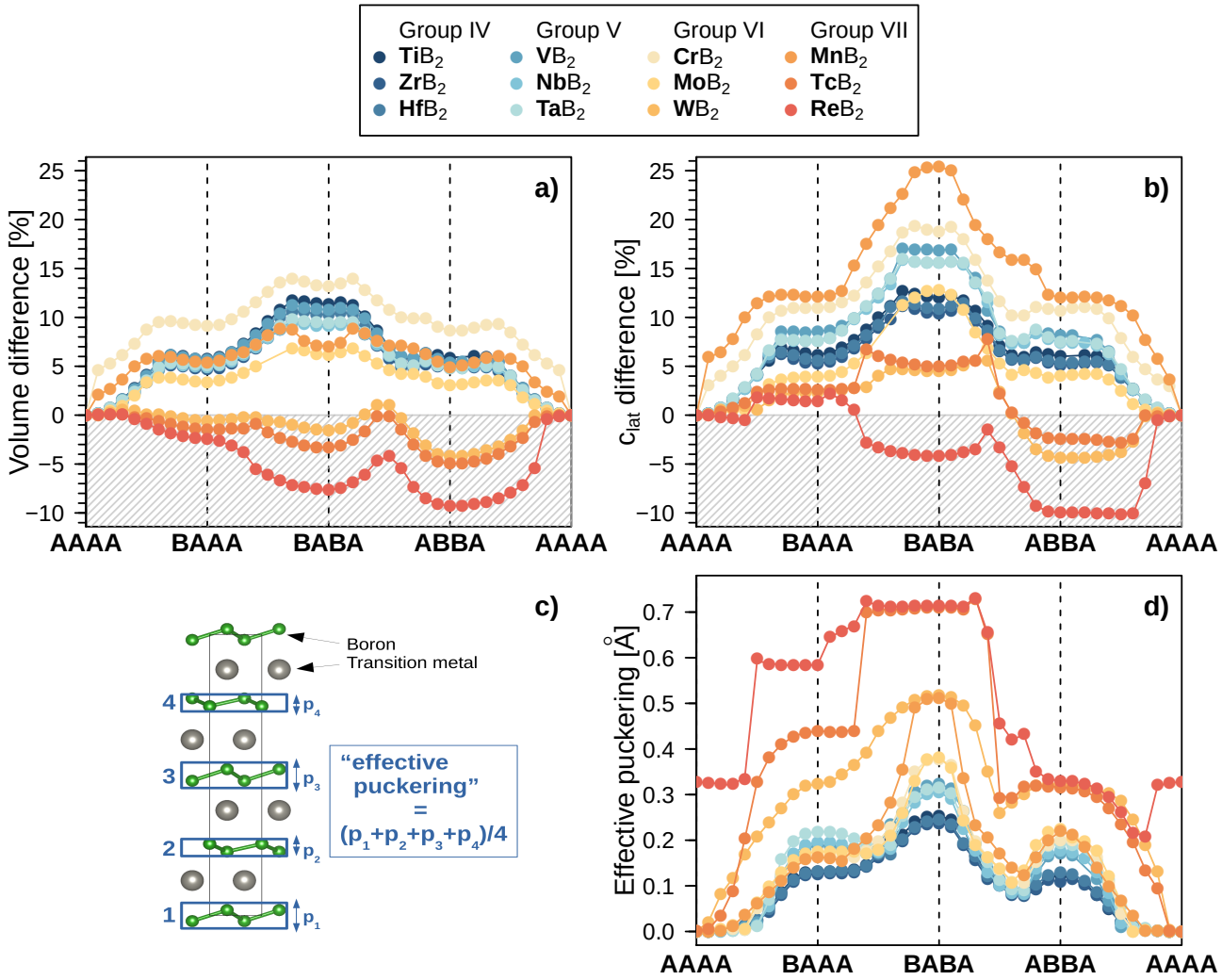


FIG. 3. (a) Volume and (b) c lattice parameter variations along the AAAA–BAAA–BABA–ABBA–AAAA transformation pathway. Positive (negative) values [%] denote relative increase (decrease) compared to the reference AAAA stacking. (c) Schematic definition of the *effective puckering* of boron planes, depicted in panel (d).

ume increase, while the AAAA→BABA TiB_2 transition enlarges volume by ≈ 11%. The AAAA stacking has the lowest volume also for CrB_2, MoB_2, and MnB_2, however, we recall its dynamical instability according to Fig. 1b. CrB_2 also shows the overall greatest volume increase along the entire pathway which, however, might stem from omitting its magnetism. Worth highlighting is the volume decrease predicted for the BAAA, BABA, and ABBA allotropes of WB_2, TcB_2, and ReB_2. We recall dynamical instability of the AAAA allotrope according to Fig. 1b. Specifically for BABA-ReB_2, the lowest-energy ReB_2 allotrope, Fig. 3a reveals a volume decrease by ≈ 8% compared to AAAA-ReB_2.

Volume changes in Fig. 3a mainly stem from the evolution of the c lattice parameter Fig. 3b, which for almost all diborides—with the exception of WB_2, TcB_2, and ReB_2—increases when leaving the perfect AAAA stacking. The lattice parameter c is parallel to the hexagonal [0001] direction, thus orthogonal to the metal/boron layers. The increase in c is compensated by relatively small lateral shrinkage (by up to 4%), i.e. lattice parameter a (= b) decrease (not shown).

Furthermore, we investigate how the different stackings of the metal planes influence the boron sublattice, in particular, the puckering of boron hexagons. Fig. 3c shows a schematic definition of the *effective puckering* (p_{eff}), calculated using the thicknesses of four boron planes in our simulation cell. Similarly to ΔE_{tot}, p_{eff} shows a strong trend following the left-to-right (group IV–VII TMB_2) and top-to-bottom (period 4–6 TMB_2) shift in the periodic table. Starting with the group IV TMB_2—TiB_2, ZrB_2, and HfB_2—the p_{eff} evolution shows essentially the same profile as ΔE_{tot}, V, and c: with similar values for the BAAA and ABBA stackings, and a peak at the least energetically stable BABA. Changing to the group V–VII TMB_2, boron layers gradually pucker more significantly,

compare, e.g. TiB_2, TaB_2, and WB_2. Such pronounced puckering is for most diborides mirrored by c lattice parameter and volume increase. Interestingly, boron plane puckering in WB_2, TcB_2, and ReB_2 is associated with a volume decrease. Furthermore, p_{eff} in the above three diborides significantly increases immediately after leaving the perfect AAAA stacking, which is consistent with high metastability/instability of the AAAA allotrope for these TMB_2.

C. Mechanical properties

Transitions between the AAAA, BAAA, ABBA, and BABA allotropes have consequences also for mechanical properties, which can be estimated via elastic constants, C_{ij}. In Fig. 4, we plot trends in polycrystalline bulk (B), shear (G), and Young's moduli (E), together with ductility estimates based on the Poisson's ratio (ν), and Cauchy pressure $C_{23} - C_{44}$ and $C_{12} - C_{66}$. Note that mechanically unstable systems (based on the criteria for elastic constants in Ref. [29]) are not shown. For the group IV–VI TMB_2s, trends in the bulk modulus (Fig. 4a) seem to resemble the energetic stability trends (Fig. 1a) in a way that the highest B is shown by the energetically most stable AAAA stacking, the lowest B for the least stable BABA stacking, and the ABBA and BAAA stackings—energetically in-between AAAA and BABA—exhibit B values between those of the AAAA and BABA stacking. Furthermore, as the energetic differences between the four allotropes diminish when going from group IV to VI, so do differences in their bulk moduli. While we do not see any clear explanation for the similarity between the total energy and bulk modulus trends, it could relate to volumetric changes in Fig. 3a, where the relative volume increase with respect to the AAAA stacking (followed by an energy increase) could induce lower resistance to compression. The overall highest bulk modulus (≈ 340 GPa) is predicted for the BABA-ReB_2, i.e. the lowest-energy ReB_2 allotrope (with $\approx 8\%$ lower volume compared to the AAAA stacking), followed by the ABBA-WB_2, i.e. the lowest-energy WB_2 allotrope (with $\approx 5\%$ lower volume compared to the AAAA stacking). Please also recall that AAAA-ReB_2 and AAAA-WB_2 are dynamically unstable. The shear and Young's moduli (Fig. 4b,c) evolve in a similar manner, differing from the relatively simple trend predicted for the bulk modulus. In particular, G (E) of the AAAA stacking decreases from $G = 256$ GPa (Ti) to $G = 106$ GPa (Re) (from $E = 580$ GPa to $E = 284$ GPa) when moving from the group IV to VII TMB_2s. In contrast, G (E) of the BABA stacking increases from $G = 125$ GPa (Ti) to $G = 276$ GPa (Re) (from $E = 312$ GPa to $E = 651$ GPa) when moving from the group IV to VII TMB_2s. Shear and Young's moduli of the ABBA and BAAA stackings show a relatively lower spread, nonetheless, increase for the group V–VI TMB_2s for which these two stackings are associated with low or almost zero energy barriers. Similar to the bulk modulus, the overall highest G and E values are predicted for BABA-ReB_2, pointing towards superior strength of this material. This is consistent with literature reports claiming ultra-incompressibility and superhardness of ReB_2 [10, 40]. Our B and G moduli yield a good agreement with *ab initio* calculated values for α-structured diborides of the group IV–VI transition metals predicted by Gu *et al.* [41].

As other ceramics, transition metal diborides are hard but suffer from brittleness which is a strong limiting factor for their fracture toughness [7]. Within the same material class, Poisson's ratio and Cauchy pressure are widely accepted empirical indicators allowing to compare two or more systems in terms of their metallic/covalent bonding character, providing a basis for more ductile/brittle behavior [42, 43]. Examples within the transition metal nitride family include Refs. [44–46]. The Poisson's ratio (Fig. 4d) of the AAAA allotrope is the lowest(≈ 0.13) for the group IV-TMB_2—TiB_2, ZrB_2, HfB_2—and significantly increases (up to ≈ 0.35) when moving to the group V, VI, and VII TMB_2s, hence, suggesting improved ductility with increased valence electron concentration (VEC). An inverse (decreasing) trend is predicted for the BABA allotrope, while the ABBA and BAAA allotropes show nearly overlapping ν values for the group IV, VI, and VII TMB_2 but differ for the group V TMB_2s. Focusing only on the lowest-energy stacking of each element, our calculations indicate similar brittleness/low ductility of TiB_2, ZrB_2, and HfB_2, which significantly improves when going VB_2, NbB_2, and TaB_2. Changing to CrB_2, ductility indicators drop again, while those of MoB_2 and WB_2 are comparable to that of TaB_2. The lowest-energy allotropes for the group VII-TMB_2 are predicted to be comparably brittle/moderately ductile as VB_2. We note that the here predicted ν values for α- and ω-structured diborides agree well with *ab initio* calculations by Moraes *et al.* [17]. In contrast to Poisson's ratio, Cauchy pressure (Fig. 4e–f) can provide a directionally-resolved indication of ductility. We recall that the Cauchy pressure of material with cubic symmetry is defined as $CP = C_{12} - C_{44}$. Since for hexagonal structures $C_{12} \neq C_{13} = C_{23}$ and $C_{44} = C_{55} \neq C_{66}$, one can define $CP_1 = C_{23} - C_{44} = C_{13} - C_{55}$ and $CP_2 = C_{12} - C_{66}$. The predicted higher CP_1 values—compared to CP_2—therefore indicate relatively more ductile (less brittle) character of the (more widely spaced) basal planes compared to the prismatic planes.

D. Electronic structure analysis

The collection of average COHP curves for all TMB_2s in the AAAA structure summarized in Fig. 5, shows trends consistent with our calculated transformation paths (Fig. 1). The stability of the AAAA stacking gradually decreases as we move to higher group TMs. This

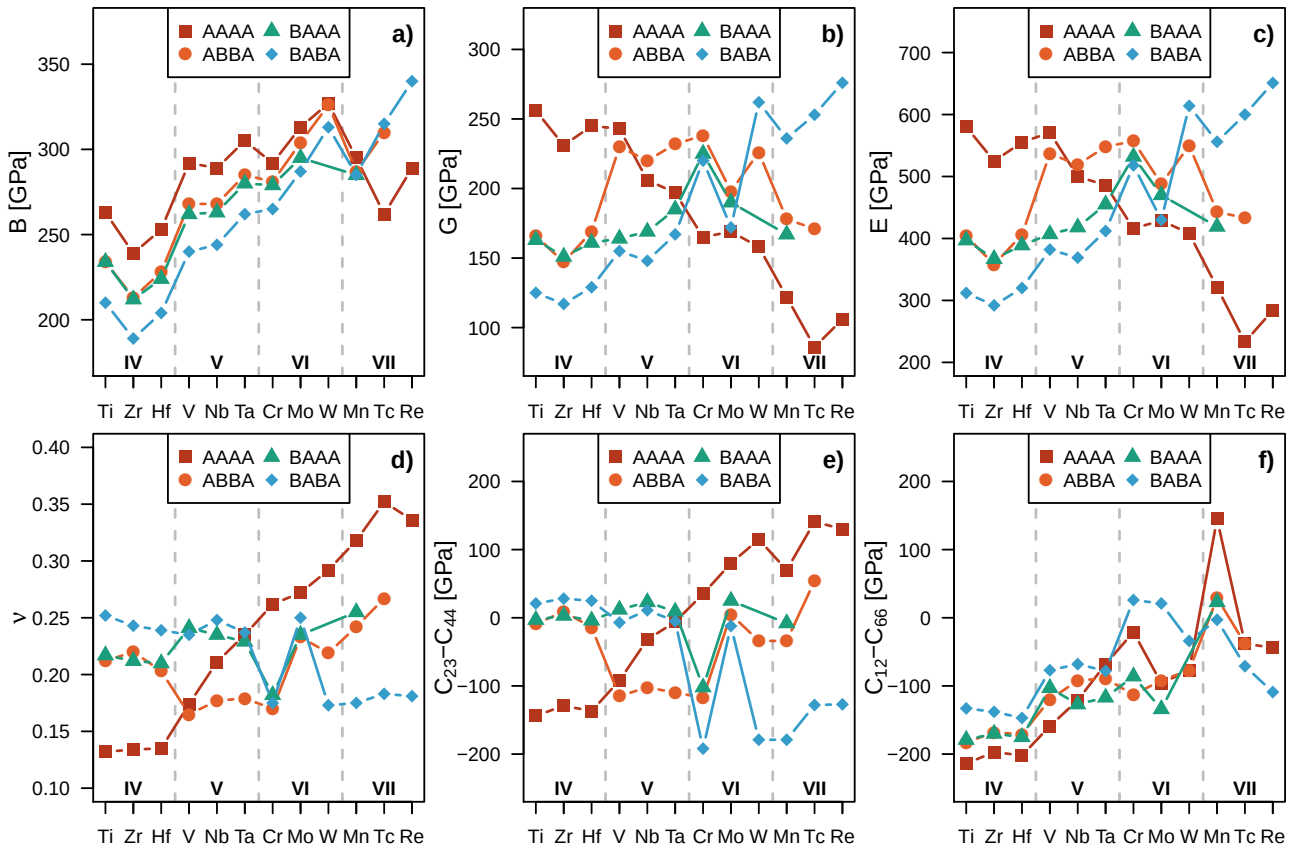


FIG. 4. Trends in mechanical properties of MB_2 structures (where M are group IV–VII transition metals) with AAAA, BAAA, ABBA, and BABA stacking sequences, as estimated based on elastic constants (C_{ij}) calculations. Polycrystalline (a) bulk, (b) shear, and (c) Young's moduli, together with ductility approximates: (d) Poisson's ratio, and Cauchy pressure, (e) $CP_1 = C_{23} - C_{44}$ and (f) $CP_2 = C_{12} - C_{66}$. Higher values indicate more metallic bonding, thus, increased tendency for ductile behavior.

fact can be explained by the occupation of antibonding (destabilizing) states as we increase the valence electron count. The COHP curves of group IV diborides contain only bonding states below the Fermi levels (E_F) while the presence of the antibonding states increases as we proceed to group VII. The preference for the AAAA stacking, therefore, downgrades in higher group TMB_2s—an observation reflected by the diminishing energy barriers between AAAA and other allotropes (see Fig. 2a–h). Additionally, when looking at ReB_2, one can notice a reduction of the antibonding states below the Fermi level in the structure, including puckering of the boron sheets (the AAAA stacking in ReB_2 prefers to pucker and translate every second layer of boron, dashed line in Fig. 5).

To elaborate on the idea of the destabilizing effect of the antibonding states, in Fig. 6 we compare TiB_2 in the AAAA (α) and BABA (γ) structures. By looking at the COHP curves we find two strong interactions, namely B-B that is bonding even above E_F and TM-B that becomes destabilizing at lower energies due to the occupation of the antibonding metal states [47, 48].

The main differences between both structures include redistribution of d_{z^2} and in-plane d_{xy,x^2-y^2} orbitals. Firstly, when going from AAAA to BABA, the d_{z^2} DOS peak (blue line in Fig. 6a and d) that is non-bonding in AAAA splits due to an interaction with B p_z (red line in Fig. 6a and d). Secondly, localization of the in-plane d orbitals (orange line in Fig. 6a and d) is enhanced in BABA due to a stronger in-plane interaction between metal atoms induced by the TM-TM bond shortening. Even though bonding in nature, the localized TM-TM peak in BABA shifts to the pseudo-gap, which results in considerably increased DOS at E_F, making the BABA structure unfavorable for early TMB_2s. To reason the stabilization of BABA in higher group TM diborides, the role of d_{z^2} orbitals was proposed to be crucial [49]. Within the AAAA structure, metal atoms positioned below the center of boron hexagons form antibonding TM-TM interaction across the boron sheets. This unfavorable interaction can be relieved by the translation of the metal atoms at positions directly below the B atoms, which also reduces the TM-B coordination from 12 to 8. Further stabilization is achieved by puckering of boron hexagons [49]. Albeit the reduction of the antibonding

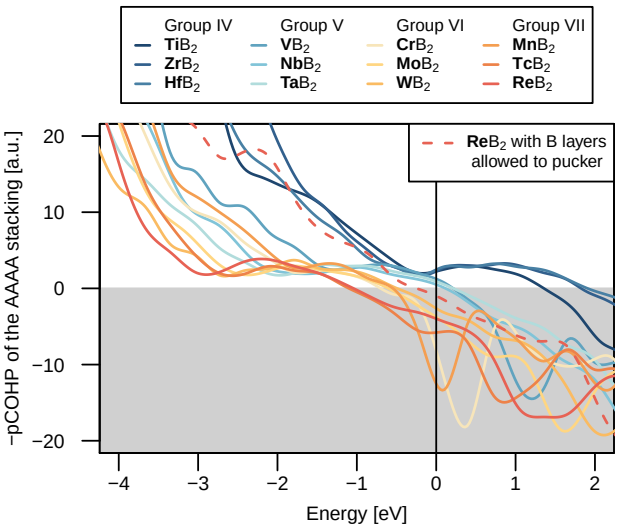


FIG. 5. Average projected COHP calculated for AAAA stacking. Negative values (gray region) correspond to destabilizing contributions.

TM-TM overlap of the d_{z^2} orbitals has a stabilizing character, the energetic contribution of this bond in negligible compared to B-B and TM-B. A charge transfer from TM to B allows for the formation of strong π bonds within the boron hexagons making the stabilizing contribution of B-B bonds greater than that of TM-B bonds.

As we move to the higher group TMs, the charge transfer reduces, and d orbitals fill up, which strengthens the TM-B bond. Consequently, TM-B bonds in early TMB_2s are longer, causing larger volume and narrower puckering of the boron sheets along the c-axis (compare with Fig. 3). The interplay between the two strongest bonds is, therefore, one of the leading parameters in the stability of TMB_2s.

Taking advantage of the rigid band approach [47–49], we can generalize the TiB_2 results to other TMB_2s. In Fig. 6a–g the dashed lines denote E_F in group IV and VII diborides. Focusing on group VII TMB_2s, the destabilization of the AAAA structure can be related to the filling of the DOS peak above the pseudo-gap with mostly metallic character that comes hand in hand with filling of the antibonding states [47], as visible in Fig. 6a–b. On the contrary, within the BABA structure the bonding/antibonding transition is shifted to higher energies.

To explain this behavior, we propose a simple molecular orbital model (Fig. 6h). First we assume the sp^2 hybridization of B atoms that consequently interact with TM atoms (grey levels on the left in Fig. 6h). The metal s electrons then interact with the σ orbitals to form the low-lying bonding region and, together with antibonding sp^2, the high energy antibonding region (black levels common to the AAAA and BABA structures). Next, the B π electrons, which are mostly of the p_z character, hybridize with TM d electrons. In the case of AAAA B p_z predominantly interacts with the out-of-plane $d_{xz,yz}$ forming the distinct covalent peak at -3 eV in TiB_2 (see also the orbital resolved COHP in the panel c). This interaction leaves d_{z^2} and in-plane d_{xy,x^2-y^2} orbitals nonbonding (the shaded region between TM bonding/antibonding states in Fig. 6h). On the other hand, in the BABA structure TM planes move and alter the stacking such that they reside at in-line positions with B atoms. This composition is favorable for a strong d_{z^2}-p_z interaction (c-axis in-line TM-B interaction in Fig. 6f) leaving both out and in-plane d orbitals non-bonding, as sketched in panel h.

In real extended systems, in-plane TM-TM interactions that were neglected in the simplistic orbital model split d orbitals into bonding and antibonding levels Fig. 6c and g). However, the position of metal atoms below the center of B hexagons in AAAA leaves the d_{z^2} levels non-bonding Fig. 6c). The metal-metal interaction in AAAA, therefore, splits only the in-plane d_{xy,x^2-y^2} orbitals contrary to the splitting of both in and out-of-plane orbitals in BABA. This effectively creates more available bonding states in BABA and shifts the bonding/antibonding turning point to higher energies. Hence filling of the d orbitals brings about stacking alternation to form short TM-B bonds and stabilizes structures with the puckered boron layers.

IV. CONCLUSIONS

We used first-principles calculations to simulate transformations between the well-known α (P6/mmm), γ ($P6_3$/mmc), and ω ($P6_6$/mmc) phase prototypes of transition metal diborides (TMB_2s). Alternating purely B and purely TM layers, the prototypes were regarded as different stackings of the TM planes, where the AAAA, BABA, and ABBA stackings correspond to the α, γ, and ω structure, respectively. Subsequently, transformations along the AAAA→BAAA→BABA→ABBA pathway were facilitated by sliding of TM layers. We discussed the predicted chemistry-related trends for the group IV–VII TMB_2s, focusing on energetics, stability, structural changes, and changes in elastic properties.

Total energy variations along the transformation pathway decrease when going from group IV to V TMB_2s, for which all stackings are found dynamically stable, with the following order of stability: AAAA<BAAA∼ABBA<BABA. The energy barriers are rather small (below 0.03 eV/at.) when moving towards the α-structure, but comparatively high (up to 0.29 eV/at.) when moving away from it, suggesting that the metastable phases easily transform to the lowest-energy α phase. The AAAA, BAAA, BABA, and ABBA allotrope change their order of stability for the group VI TMB_2s and, moreover, the AAAA stacking becomes dynamically unstable. The ABBA variant is predicted to be the most stable phase prototype for both MoB_2 and WB_2. For the group VII TMB_2s, the AAAA allotrope remains dynamically unstable. While MnB_2 energetically prefers the ABBA stackings, it exhibits low energy bar-

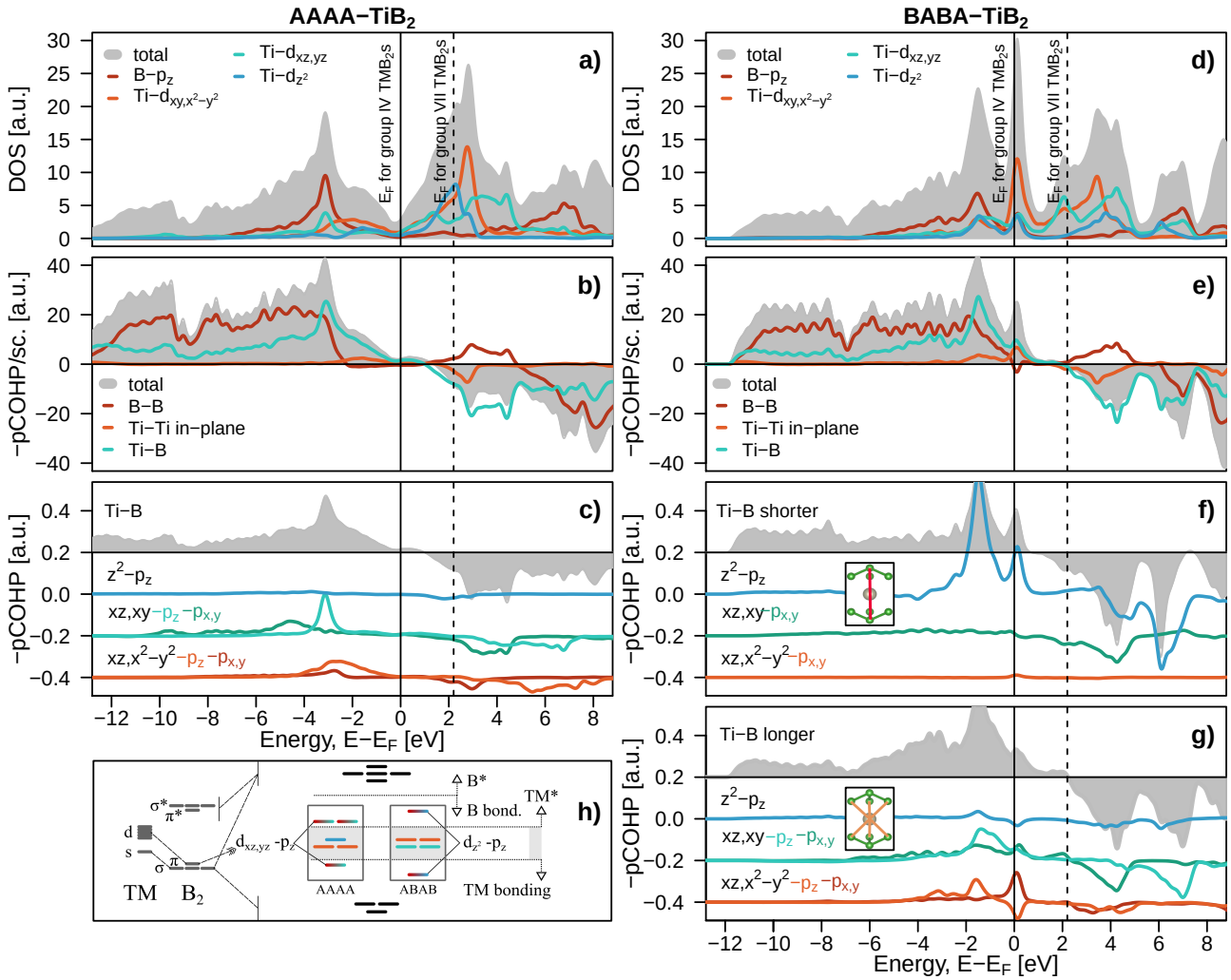


FIG. 6. For TiB_2 in AAAA structure calculated (a) DOS, (b) total projected COHP, (c) TM-B (2.38Å) orbital resolved projected COHP/bond. Calculations in BABA structure: (d) DOS, (e) total projected COHP and orbital resolved projected COHP/bond for (f) shorter TM-B (2.24Å) and (g) longer TM-B (2.42Å). (h) Suggested MO diagram for TMB_2. The gray area for non-bonding TM levels, the asterisk denotes antibonding states. Colors of d states match local DOS in panels a,d..

riers (around 0.1 eV/at.) for the other two dynamically stable allotropes. Unlike that, TcB_2 and ReB_2 show deep global energy minima at the BABA stacking, yielding high energy barriers for the BAAA and ABBA allotrope (about 0.30-0.45 eV/at.).

The AAAA↔BAAA↔BABA↔ABBA transformations also lead to volumetric changes, mainly stemming from changes of the c lattice parameter, i.e. relaxations along the [0001] direction. These can be traced down to the puckering of the boron planes between the metal layers. Mirroring the dynamical instability of the α structure for the group VI–VII TMB_2, boron layers start to pucker already when one of the transition metal layers is slightly shifted from the ideal AAAA stacking. WB_2, TcB_2 and ReB_2 are particularly interesting, since their BAAA, BABA, and ABBA allotropes yield a volume decrease compared to the AAAA stacking, despite of highly puckered boron layers which should, intuitively, take more space than the flat AAAA arrangement.

The relative order of volumes corresponding to the four diboride allotropes also seems to inversely correlate with their bulk moduli, meaning that TMB_2 stackings with higher volume exhibit lower bulk modulus. The overall highest B, G, and E moduli are predicted for BABA-ReB_2, pointing towards excellent strength. The calculated Poisson's ratio and the Cauchy pressure indicate changes in ductility when moving from group IV to group VII TMB_2s but also depending on the stacking of the transition metal planes. Specifically, ductility increases with increasing VEC for the α-structure and decreases with VEC for the γ-structure, while a minimum in ductility in the ω-structure is predicted for group V TMB_2s. Filling of the d orbitals in higher group TMs weakens the B-B bonds, increases the preference to form strong

TM-B bonds, and raises the DOS at E_F in the AAAA allotrope. The combination of previous observations supports structural relaxation that moves TM in line with B to utilizing d_{z^2}-p_z hybridization to split the non-bonding d_{z^2} DOS peak at E_F. The increasing preference for the TM-B interaction over B-B causes boron sheets to pucker to reduce TM-B distance.

ACKNOWLEDGEMENTS

NK acknowledges the Hertha Firnberg fellowship by Austrian Science Fund, FWF, (T30801). Computational resources were provided by the Vienna Scientific Cluster (VSC), the cluster at the Montanuniversität Leoben (MUL-hpc), and by Swedish National Infrastructure for Computing (SNIC), on the Clusters located at the National Supercomputer Centre (NSC) in Linköping, the Center for High Performance Computing (PDC) in Stockholm, and at the High Performance Computing Center North (HPC2N) in Umeå, Sweden. This work has been partially supported by the Spanish Ministry of Science and Innovation with PID2019-105488GB-I00 (JJ).

[1] C. Fuger, V. Moraes, R. Hahn, H. Bolvardi, P. Polcik, H. Riedl, and P. H. Mayrhofer, Influence of Tantalum on phase stability and mechanical properties of WB_2, MRS Communications **9**, 375 (2019).

[2] C. Fuger, R. Hahn, L. Zauner, T. Wojcik, M. Weiss, A. Limbeck, O. Hunold, P. Polcik, and H. Riedl, Anisotropic super-hardness of hexagonal $WB_{2\pm z}$ thin films, Materials Research Letters **10**, 70 (2022).

[3] J. Palisaitis, M. Dahlqvist, L. Hultman, I. Petrov, J. Rosen, and P. O. Persson, On the nature of planar defects in transition metal diboride line compounds, Materialia **24**, 101478 (2022).

[4] J. Palisaitis, M. Dahlqvist, A. J. Hall, J. Thörnberg, I. Persson, N. Nedfors, L. Hultman, J. E. Greene, I. Petrov, J. Rosen, and P. O. Persson, Where is the unpaired transition metal in substoichiometric diboride line compounds?, Acta Materialia **204**, 116510 (2021).

[5] V. Šroba, T. Fiantok, M. Truchlý, T. Roch, M. Zahoran, B. Grančič, P. Švec, Š. Nagy, V. Izai, P. Kúš, and M. Mikula, Structure evolution and mechanical properties of hard tantalum diboride films, Journal of Vacuum Science & Technology A: Vacuum, Surfaces, and Films **38**, 033408 (2020).

[6] B. Paul, N. L. Okamoto, M. Kusakari, Z. Chen, K. Kishida, H. Inui, and S. Otani, Plastic deformation of single crystals of CrB_2, TiB_2 and ZrB_2 with the hexagonal AlB_2 structure, Acta Materialia **211**, 116857 (2021).

[7] M. Magnuson, L. Hultman, and H. Högberg, Review of transition-metal diboride thin films, Vacuum **196**, 110567 (2022).

[8] C. Mitterer, Borides in thin film technology, Journal of solid state chemistry **133**, 279 (1997).

[9] C. Liu, X. Gu, K. Zhang, W. Zheng, Y. Ma, and C. Chen, Superhard metallic compound TaB_2 via crystal orientation resolved strain stiffening, Physical Review B **105**, 024105 (2022).

[10] H.-Y. Chung, M. B. Weinberger, J. B. Levine, A. Kavner, J.-M. Yang, S. H. Tolbert, and R. B. Kaner, Synthesis of ultra-incompressible superhard rhenium diboride at ambient pressure, Science **316**, 436 (2007).

[11] J. Nagamatsu, N. Nakagawa, T. Muranaka, Y. Zenitani, and J. Akimitsu, Superconductivity at 39 K in magnesium diboride, Nature **410**, 63 (2001).

[12] N. Hellgren, A. Sredenschek, A. Petruins, J. Palisaitis, F. F. Klimashin, M. A. Sortica, L. Hultman, P. O. Persson, and J. Rosen, Synthesis and characterization of TiB_x ($1.2\leq x \leq 2.8$) thin films grown by DC magnetron co-sputtering from TiB_2 and Ti targets, Surface and Coatings Technology **433**, 128110 (2022).

[13] B. Bakhit, J. Palisaitis, J. Thörnberg, J. Rosen, P. O. Persson, L. Hultman, I. Petrov, J. E. Greene, and G. Greczynski, Improving the high-temperature oxidation resistance of TiB_2 thin films by alloying with al, Acta Materialia **196**, 677 (2020).

[14] R. G. Munro, Material properties of titanium diboride, Journal of Research of the National institute of standards and Technology **105**, 709 (2000).

[15] X. Y. Wang C, Song L, Mechanical and electrical characteristics of wb_2 synthesized at high pressure and high temperature, Materials (Basel) **13**, 1212 (2020).

[16] S. J. La Placa and B. Post, The crystal structure of rhenium diboride, Acta Crystallogr. **15**, 97 (1962).

[17] V. Moraes, H. Riedl, C. Fuger, P. Polcik, H. Bolvardi, D. Holec, and P. H. Mayrhofer, Ab initio inspired design of ternary boride thin films, Scientific Reports **8**, 1 (2018).

[18] R. Kiessling, A. Wetterholm, L. G. Sillén, A. Linnasalmi, and P. Laukkanen, The crystal structures of molybdenum and tungsten borides, Acta Chem. Scand. **1**, 893 (1947).

[19] R. F. Zhang, D. Legut, R. Niewa, A. S. Argon, and S. Veprek, Shear-induced structural transformation and plasticity in ultraincompressible ReB_2 limit its hardness, Phys. Rev. B Condens. Matter **82**, 104104 (2010).

[20] B. Hunter, X.-X. Yu, N. De Leon, C. Weinberger, W. Fahrenholtz, G. Hilmas, M. L. Weaver, and G. B. Thompson, Investigations into the slip behavior of zirconium diboride, J. Mater. Res. **31**, 2749 (2016).

[21] B. Paul, N. L. Okamoto, M. Kusakari, Z. Chen, K. Kishida, H. Inui, and S. Otani, Plastic deformation of single crystals of CrB_2, TiB_2 and ZrB_2 with the hexagonal AlB_2 structure, Acta Mater. **211**, 116857 (2021).

[22] G. Kresse and J. Furthmüller, Efficient iterative schemes for *ab initio* total-energy calculations using a plane-wave basis set, Physical Review B **54**, 11169 (1996).

[23] G. Kresse and D. Joubert, From ultrasoft pseudopotentials to the projector augmented-wave method, Physical

Review B **59**, 1758 (1999).
[24] J. P. Perdew, K. Burke, and M. Ernzerhof, Generalized gradient approximation made simple, Physical review letters **77**, 3865 (1996).
[25] T. Bučko, J. Hafner, and J. Ángyán, Geometry optimization of periodic systems using internal coordinates, The Journal of Chemical Physics **122**, 124508 (2005).
[26] Y. Le Page and P. Saxe, Symmetry-general least-squares extraction of elastic data for strained materials from ab initio calculations of stress, Physical Review B **65**, 104104 (2002).
[27] Y. Le P. and P. Saxe, Symmetry-general least-squares extraction of elastic coefficients from *ab initio* total energy calculations, Physical Review B **63**, 174103 (2001).
[28] R. Yu, J. Zhu, and H. Q. Ye, Calculations of single-crystal elastic constants made simple, Comput. Phys. Commun. **181**, 671 (2010).
[29] F. Mouhat and F.-X. Coudert, Necessary and sufficient elastic stability conditions in various crystal systems, Physical Review B **90**, 224104 (2014).
[30] J. F. Nye, *Physical properties of crystals: their representation by tensors and matrices* (Oxford University Press, 1985).
[31] R. Hill, The elastic behaviour of a crystalline aggregate, Proceedings of the Physical Society. Section A **65**, 349 (1952).
[32] A. Togo, F. Oba, and I. Tanaka, First-principles calculations of the ferroelastic transition between rutile-type and $CaCl_2$-type SiO_2 at high pressures, Physical Review B **78**, 134106 (2008).
[33] R. Dronskowski and P. E. Blöchl, Crystal orbital hamilton populations (COHP): energy-resolved visualization of chemical bonding in solids based on density-functional calculations, The Journal of Physical Chemistry **97**, 8617 (1993)
[34] S. Maintz, V. L. Deringer, A. L. Tchougréeff, and R. Dronskowski, Analytic projection from plane-wave and PAW wavefunctions and application to chemical-bonding analysis in solids, Journal of Computational Chemistry **34**, 2557 (2013)
[35] S. Maintz, V. L. Deringer, A. L. Tchougréeff, and R. Dronskowski, LOBSTER: A tool to extract chemical bonding from plane-wave based DFT (2016)
[36] L.-P. Ding, P. Shao, F.-H. Zhang, C. Lu, L. Ding, S. Y. Ning, and X. F. Huang, Crystal structures, stabilities, electronic properties, and hardness of MoB_2: First-principles calculations, Inorganic Chemistry **55**, 7033 (2016).
[37] The Materials Project, Materials data on CrB_2 by Materials Project 10.17188/1207357 (2020)
[38] The Materials Project, Materials data on MnB_2 by Materials Project 10.17188/1277089 (2020)
[39] X. Hao, Y. Xu, Z. Wu, D. Zhou, X. Liu, X. Cao, and J. Meng, Low-compressibility and hard materials Reb_2 and Wb_2: Prediction from first-principles study, Phys. Rev. B **74**, 224112 (2006).
[40] J. Levine, J. Betts, J. Garrett, S. Guo, J. Eng, A. Migliori, and R. Kaner, Full elastic tensor of a crystal of the superhard compound ReB_2, Acta Materialia **58**, 1530 (2010).
[41] X. Gu, C. Liu, H. Guo, K. Zhang, and C. Chen, Sorting transition-metal diborides: New descriptor for mechanical properties, Acta Materialia **207**, 116685 (2021).
[42] G. N. Greaves, A. L. Greer, R. S. Lakes, and T. Rouxel, Poisson's ratio and modern materials, Nature Materials **10**, 823 (2011).
[43] D. Pettifor, Theoretical predictions of structure and related properties of intermetallics, Materials Science and Technology **8**, 345 (1992).
[44] N. Koutná, A. Brenner, D. Holec, and P. H. Mayrhofer, High-throughput first-principles search for ceramic superlattices with improved ductility and fracture resistance, Acta Materialia **206**, 116615 (2021).
[45] D. G. Sangiovanni, V. Chirita, and L. Hultman, Electronic mechanism for toughness enhancement in $Ti_xM_{1-x}N$ (M=Mo and W), Physical Review B **81**, 104107 (2010).
[46] K. Balasubramanian, S. V. Khare, and D. Gall, Valence electron concentration as an indicator for mechanical properties in rocksalt structure nitrides, carbides and carbonitrides, Acta Materialia **152**, 175 (2018).
[47] X.-Q. Chen, C. L. Fu, M. Krčmar, and G. S. Painter, Electronic and structural origin of ultraincompressibility of 5*d* transition-metal diborides MB_2 (M=W, Re, Os), Physical Review Letters **100**, 196403 (2008)
[48] N. Wang, Z. Fu, D. Legut, B. Wei, T. C. Germann, and R. Zhang, Designing ultrastrong 5*d* transition metal diborides with excellent stability for harsh service environments, Physical Chemistry Chemical Physics **21**, 16095 (2019)
[49] J. K. Burdett, E. Canadell, and G. J. Miller, Electronic structure of transition-metal borides with the AlB_2 structure, Journal of the American Chemical Society **108**, 6561 (1986)